PERFORMANCE OF A MICROWAVE ANTENNA SYSTEM IN THE SHOULDER REGION OF A BLUNT REENTRY NOSE CONE

J. Leon Poirier, et al

Air Force Cambridge Research Laboratories
L. G. Hanscom Field, Massachusetts

24 October 1973

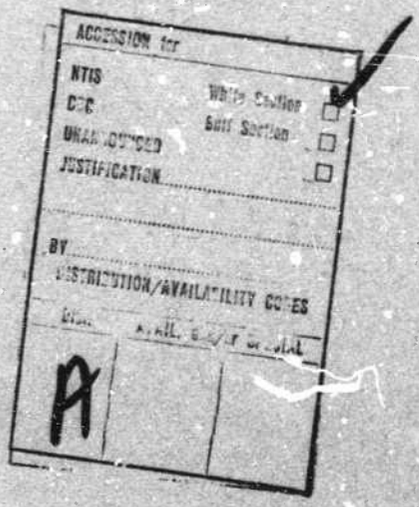

Unclassified
Security Classification

AD777828

DOCUMENT CONTROL DATA - R & D

(Security classification of title, body of abstract and indexing annotation must be entered when the overall report is classified)

1. ORIGINATING ACTIVITY *(Corporate author)*
Air Force Cambridge Research Laboratories (LZP)
L. G. Hanscom Field
Bedford, Massachusetts 01730

2a. REPORT SECURITY CLASSIFICATION
Unclassified

2b. GROUP

3. REPORT TITLE
PERFORMANCE OF A MICROWAVE ANTENNA SYSTEM IN THE SHOULDER REGION OF A BLUNT REENTRY NOSE CONE

4. DESCRIPTIVE NOTES *(Type of report and inclusive dates)*
Scientific. Interim.

5. AUTHOR(S) *(First name, middle initial, last name)*
J. Leon Poirier
John D. Antonucci
David H. Tropea

6. REPORT DATE	7a. TOTAL NO. OF PAGES	7b. NO. OF REFS
24 October 1973	43	16

8a. CONTRACT OR GRANT NO.		9a. ORIGINATOR'S REPORT NUMBER(S)
b. PROJECT, TASK, WORK UNIT NOS.	46420101	AFCRL-TR-73-0656
c. DOD ELEMENT	681000	9b. OTHER REPORT NO(S) *(Any other numbers that may be assigned this report)*
d. DOD SUBELEMENT	62101F	PSRP No. 570

10. DISTRIBUTION STATEMENT
Approved for Public Release; distribution unlimited.

11. SUPPLEMENTARY NOTES	12. SPONSORING MILITARY ACTIVITY
TECH, OTHER	Air Force Cambridge Research Laboratories (LZP) L. G. Hanscom Field Bedford, Massachusetts 01730

13. ABSTRACT

The purpose of the third AFCRL Trailblazer II reentry vehicle flight was to study the effects of shock ionized air on the performance of a microwave antenna system located in the expansion region of the nose cone. The system consisted of a pair of cavity-backed circumferential slot antennas mounted one behind the other on the conical afterbody of the reentry vehicle. During reentry, measurements of antenna impedance mismatch, interantenna coupling, signal attenuation and antenna pattern distortion were made. The data have been compared with computed values and found to be in good agreement. This experiment thus establishes the validity of the various microwave and flow field models and calculations used to obtain the theoretical values in the shoulder region of the reentry body. These results will now serve as a standard against which to compare the properties of various chemical alleviants which are being studied in other flights.

DD FORM 1 NOV 65 1473

Unclassified
Security Classification

Unclassified

Security Classification

14. KEY WORDS	LINK A		LINK B		LINK C	
	ROLE	WT	ROLE	WT	ROLE	WT
Plasma						
Reentry flight test						
Microwave flight test measurements						

Unclassified

Security Classification

Preface

The authors wish to acknowledge the efforts of the many individuals who contributed to the success of this flight. The flight program was under the supervision of Walter Rotman, Chief of the Plasma Electromagnetics Branch. Special recognition is given to R. Walters of AFCRL and R. Sukys of Northeastern University. Mr. Walters was responsible for the mechanical design and testing of the payload and its final installation into the launch vehicle. Mr. Sukys was responsible for the design of many of the electronic systems and signal processing circuits.

There were many additional people involved in various degrees during the planning, designing, constructing, launching, and data reduction of the nose cone. Among these were R. Symmes of Northeastern University, N. Karas, and Dr. D. Hayes of AFCRL. The AFCRL machine shop facilities fabricated the mechanical hardware, diagnostic probes, and microwave antennas for the experiment. Much of this work was done by W. Mathison. Our thanks are also extended to the NASA Flight Test Facility at Wallops Island, Virginia, for their help and cooperation in the launching of the vehicle.

Finally, we wish to thank J. Lennon for supplying the plasma profiles and Dr. R. Fante for the plasma covered antenna computations.

Contents

1.	INTRODUCTION	7
2.	DESCRIPTION OF VEHICLE AND EXPERIMENT	8
3.	VEHICLE FLIGHT PERFORMANCE	15
4.	S-BAND TEST SYSTEM	19
	4.1 Introduction	19
	4.2 Antenna System Performance in a Plasma	23
	4.3 Computation of Theoretical Values	25
5.	FLIGHT TEST RESULTS	30
6.	SUMMARY	40
REFERENCES		41
APPENDIX A: Slot Aperture Radiation Fields		43

Illustrations

1.	Trailblazer II Vehicle on Launcher	9
2.	General Features of a Typical Trailblazer II Trajectory	11
3.	Reentry Nose Cone	11
4.	Block Diagram of Payload	12

Illustrations

5.	Head-on View of the Nose Cone Showing the Location of the Antennas and Probes	13
6.	Flight Trajectory Showing Significant Events	16
7.	Time History of Altitude and Velocity	17
8.	Frequency of Cyclic Variations in Test Data	17
9.	Decay of Angle of Attack During Reentry	18
10.	Geographical Orientation of Vehicle to Ground Stations During Descent	18
11.	Block Diagram of S-Band Test System	20
12.	Photo of S-Band System Components	20
13.	Cutaway View of Vehicle Surface Showing S-Band Test System	21
14.	Sketch of Test Antenna	22
15.	Coordinate System for Slot Antenna on an Infinite Ground Plane	27
16.	Coordinate System for Slot Antenna on Reentry Nose Cone	27
17.	Comparison of Computed Pattern for Slot or Flat Ground Plane and Measured Pattern for Reentry Nose Cone	28
18.	Computed "Amplitude Patterns" for Plasma Covered Slot Antenna	30
19.	Power Reflection Coefficient	31
20.	Plasma Induced Reflection Loss	32
21.	Interantenna Coupling Loss	32
22.	External Coupling Loss	33
23.	Composite Signal Attenuation	34
24.	Composite Signal Attenuation	36
25.	Comparison of Composite Signal Attenuations of Front Lobe and Back Lobe	39

Tables

1.	Antenna and Probe Locations and Identifications	14
2.	Vehicle and Flight Parameters for Third Flight	16
3.	Test Antenna Dimensions and Physical Characteristics	22
4.	Plasma Properties at Test Antenna Body Location	29

Performance of a Microwave Antenna System in the Shoulder Region of a Blunt Reentry Nose Cone

1. INTRODUCTION

This report represents an analysis of data obtained during the third flight in a continuing series of experiments flown by AFCRL aboard Trailblazer II rockets. Details on other flights in the series can be found in separately published reports.[1-5] The over-all purpose of the program is twofold: The first three flights have been devoted to the study of the effects of the plasma sheath on microwave systems, whereas the remaining ones involve methods of eliminating the radio blackout and other adverse effects that generally occur during the hypersonic reentry of aerospace vehicles.

(Received for publication 24 October 1973)

1. Poirier, J.L., Rotman, W., Hayes, D.T., and Lennon, J.F. (1969) Effects of the Reentry Plasma Sheath on Microwave Antenna Performance: Trailblazer II Rocket Results of 18 June 1967, AFCRL-69-0354.

2. Hayes, D.T. (1972) Electrostatic probe measurements of flow field characteristics of a blunt body reentry vehicle. Presented at 5th Fluid and Plasma Dynamics Conference, Boston, Mass., AIAA Paper 72-694.

3. Hayes, D.T., Herskovitz, S.B., Lennon, J.F., and Poirier, J.L. (1972) Preliminary Report on the Trailblazer II Chemical Alleviation Flight of 28 July 1972, AFCRL-72-0640.

4. Rotman, W., and Maloney, L.R. (1973) High Power Microwave Antenna Performance in the Stagnation Region of a Blunt Reentry Nose Cone, AFCRL-TR-73-0072.

5. Hayes, D.T., and Rotman W. (1973) Microwave and electrostatic probe measurements and a blunt reentry vehicle, AIAA Journal 11(No. 5):675.

On the first two flights, the microwave measurements of plasma effects were confined to the stagnation region at the nose of the vehicle. Here the flow of high temperature gases in the shock layers formed by the vehicle is more symmetrical and easier to calculate. Hence the analysis of a microwave antenna system that depends on the detail knowledge of the flow over the antenna is more easily carried out. Thus meaningful comparisons between theory and measurement can be made.

In contrast, the present flight involves microwave antenna systems located on the conical afterbody where the envelope of ionized gases undergoes expansion and cooling. The flow here can no longer be considered strictly axisymmetric since the vehicle enters at an angle of attack. As a result, the analysis of plasma-signal interactions is considerably more complex.

On all flights, the microwave experiments were accompanied by subsidiary diagnostic probes designed to produce independent corroboration of the plasma and its effects. On previous flights, electroacoustic probes[6] and electrostatic probes have been used. The latter, the most successful, were also included on the present flight along with a strip line probe[7] and a dual element conductivity probe.[8]

However, the present experiment was principally concerned with the radiating characteristics of the S-band antennas on the shoulder of the vehicle, therefore only the information from this system will be analyzed in the report; in particular, the modification of the antenna radiation pattern, the antenna impedance mismatch, the interantenna coupling, and the signal attenuation due to the plasma sheath during the flight will be presented in detail.

A knowledge of the experimental conditions is necessary in order to place the results in context. For this reason, a general description of the vehicle and experiment is first presented in Section 2.

2. DESCRIPTION OF VEHICLE AND EXPERIMENT

The reentry nose cone is launched on a Trailblazer II vehicle, Figure 1, a four-stage solid-propellant rocket. After the first two stages drive the vehicle to an altitude of about 200 miles, the last two stages propel the reentry nose cone back toward the atmosphere in an almost vertical trajectory. During ascent, the vehicle is fin-stabilized. Shortly after launch, the canted second-stage fins

---

6. Lustig, C.D., and Hayes, D.T. (1969) Observation of electroacoustic resonance in a reentry sheath, Proc. IEEE 57(No. 5):800-802.
7. Karas, N.V. (1972) Microstrip Plasma Probe, AFCRL-72-0417.
8. Aisenberg, S., and Chang, K.W. (1971) Chemical Additives and Diagnostics for High Temperature Air Plasmas, AFCRL-62-0354, Final Report, Contract F19628-71-C-0077.

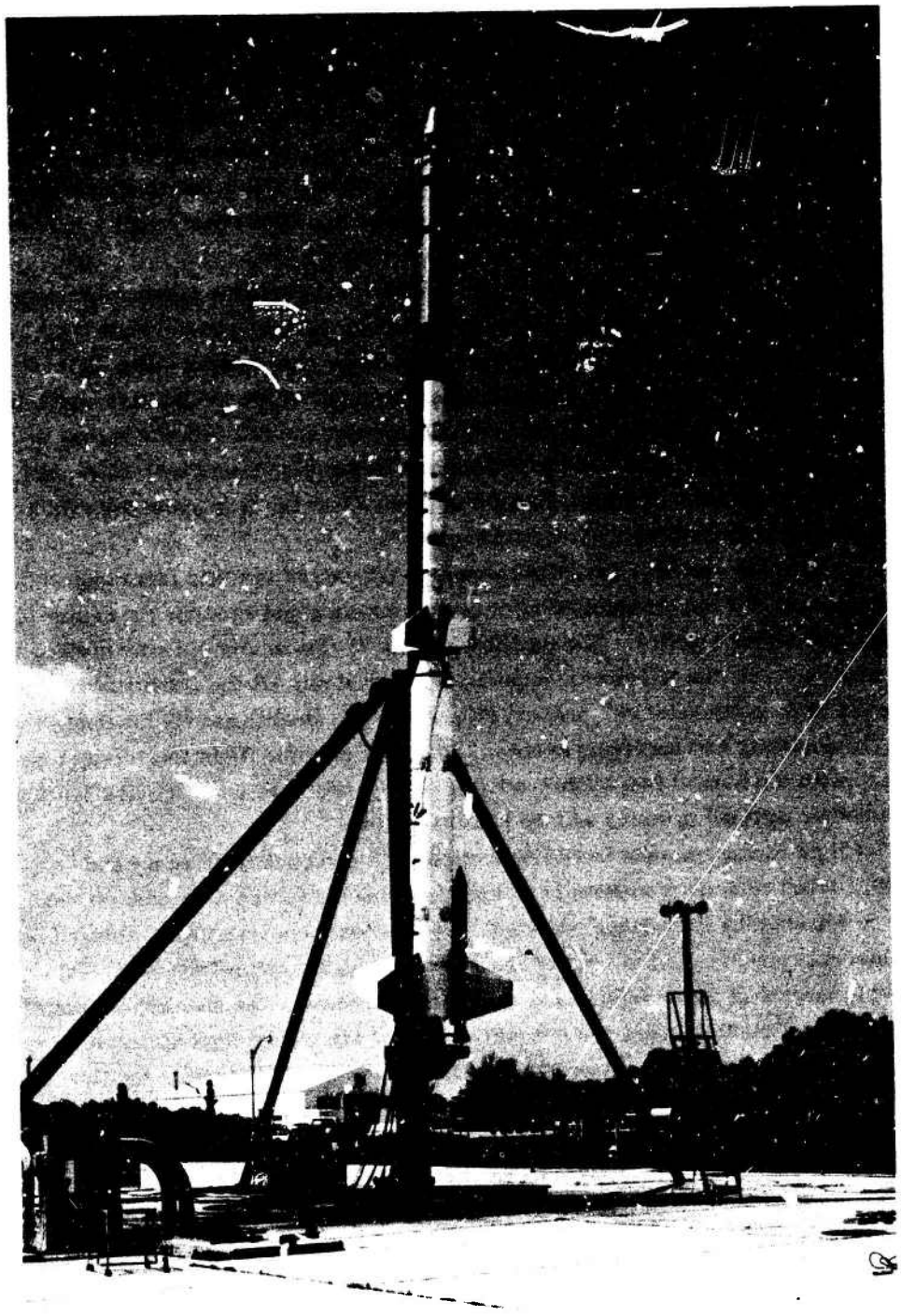

Figure 1. Trailblazer II Vehicle on Launcher

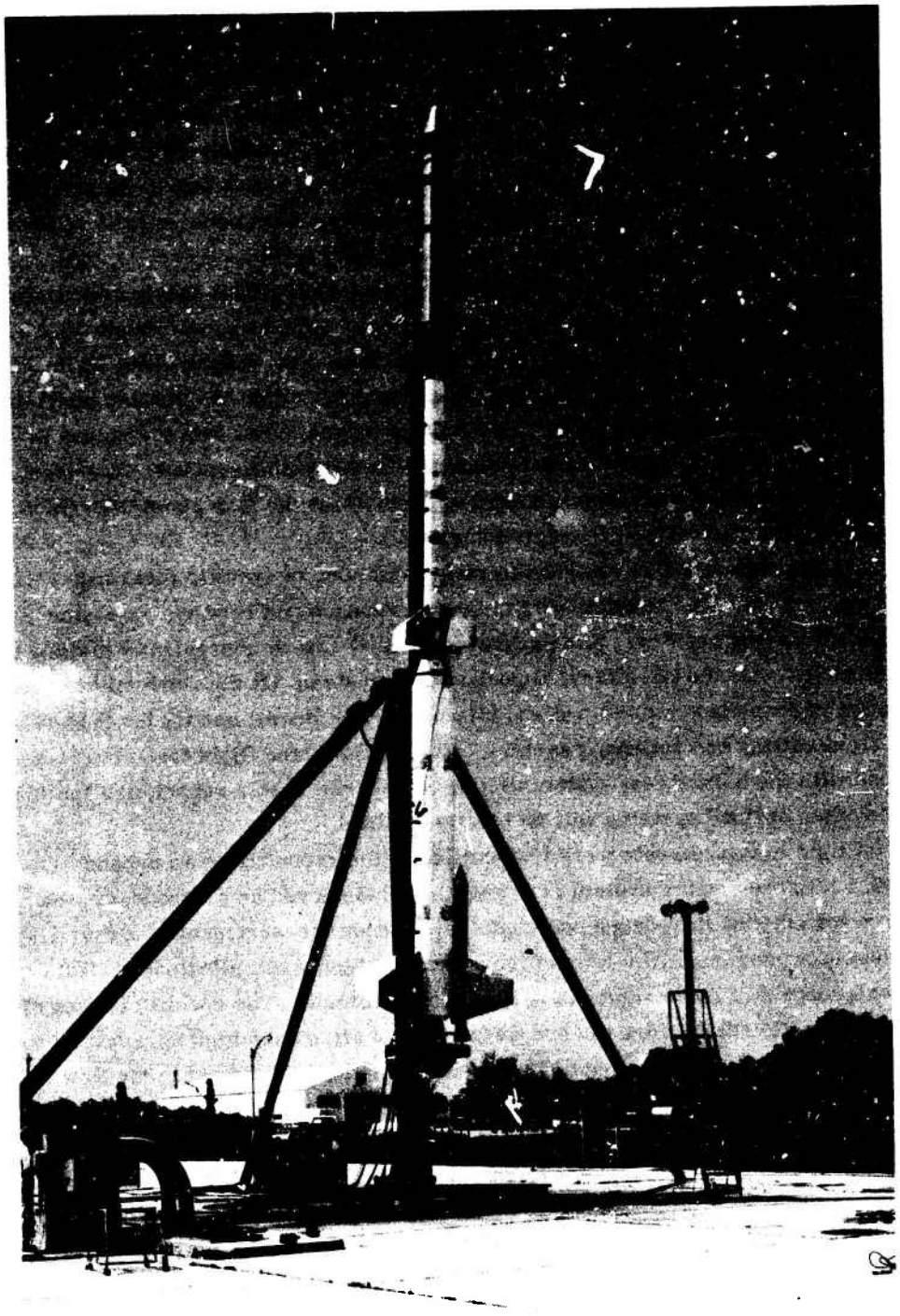

Figure 1. Trailblazer II Vehicle on Launcher

induce spinning, and as the vehicle leaves the atmosphere, its spin rate is high enough to ensure that it will be spin-stabilized through the remainder of the flight.

The last two stages are enclosed in a structural shell (velocity package), facing rearward during launch (Figure 2). At about 250 kft, the velocity package separates from the spent second-stage motor and coasts to apogee. As the velocity package begins its descent, the X-248 third-stage motor fires, propelling the reentry nose cone out of the open end of the velocity package. The 15-inch fourth-stage spherical motor provides the final thrust necessary to boost the nose cone velocity to about 17,000 fps by the time it reaches the start of reentry.

The reentry nose cone (Figure 3) is a 9^{o} hemisphere-cone fabricated entirely of aluminum. Its dimensions are: nose cap radius 6.33 in.; total length 26.47 in.; and base diameter 19.17 in. The instrumented nose cone weighs about 72 lb including the spent fourth-stage motor which remains within the reentry body. In order that the measured plasma properties can be compared with the values predicted from clean-air flow-field calculations, the heat-sink method of thermal protection (no ablative coatings) is used to ensure that the flow about the vehicle is not contaminated with ablation products.

The experiment was designed to make a number of specific measurements of the plasma and the behavior of microwave radiating and receiving systems before and during reentry. The payload (Figure 4) can be conveniently divided into five sections: (1) the telemetry/secondary test system; (2) the conductivity probe; (3) a set of four electrostatic probes; (4) a strip-line probe; and (5) the S-band test transmitting and receiving system. Although only the flight test results concerned with the S-band test system will be considered in this report, the function of the other payload systems will be briefly outlined.

Flight measurements were transmitted to the ground over an S-band (2220.5 MHz) telemetry system (TX/TM) that also served as a secondary test source for antenna impedance and signal attenuation measurements. Description of plasma properties at the rear of the vehicle is highly complicated; analysis of performance of these antennas is thus more difficult. The specific causes of the complex flow field were the non-zero angle of attack and high spin rate of the vehicle. This introduced asymmetry which was quite pronounced in the flow at the back of the vehicle.[9] In addition, the flow at the back of the nose cone is undergoing transition to wake conditions. Because of these factors, analysis of data from the telemetry system will be carried out later and presented in a future report.

---

9. Lennon, J.F. (1972) Trailblazer II Rocket Tests on the Reentry Plasma Sheath: Vehicle Performance and Plasma Predictions (Flights No. 1-3), AFCRL-TR-73-0317.

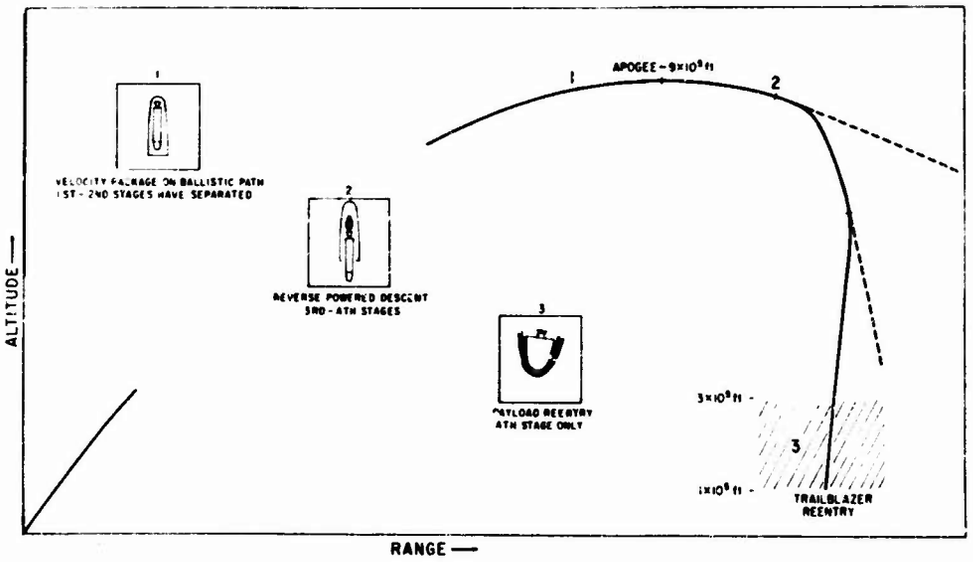

Figure 2. General Features of Typical Trailblazer II Trajectory

Figure 3. Reentry Nose Cone

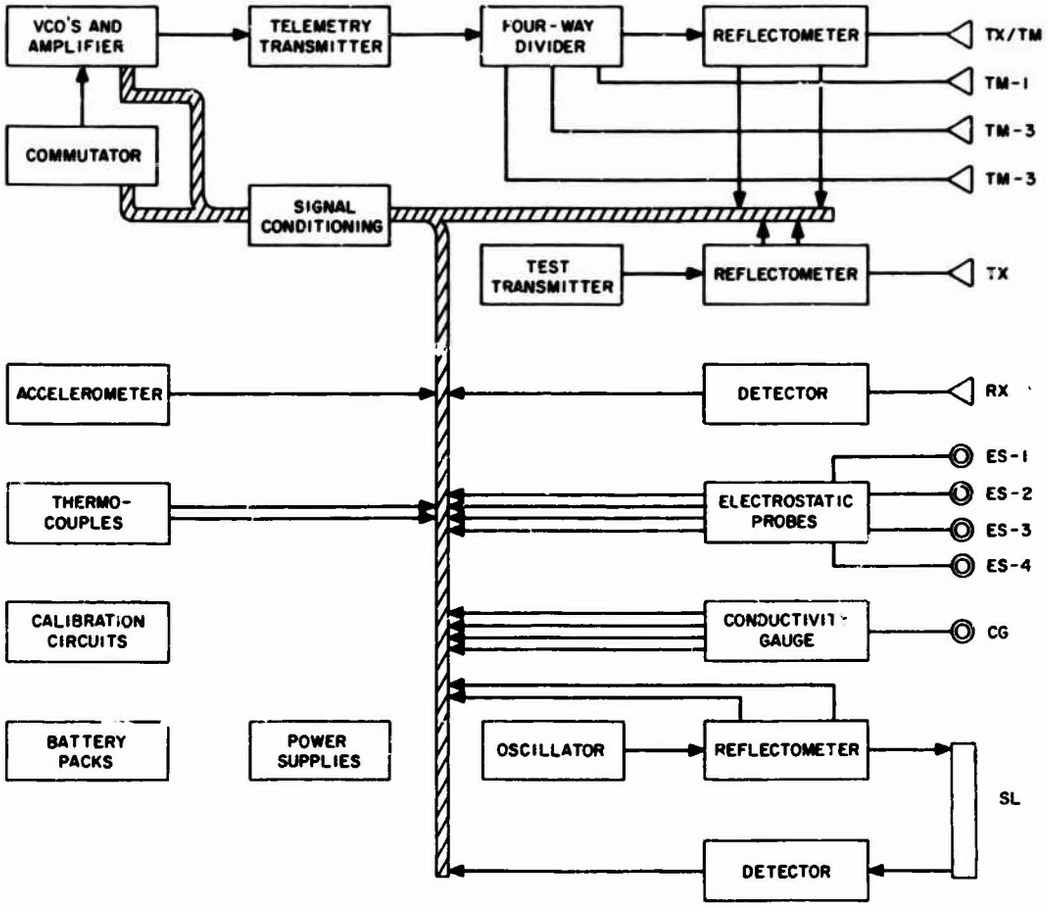

Figure 4. Block Diagram of Payload

The conductivity gauge had a flush-mounted probe located at the shoulder of the vehicle. The plasma properties were to be determined by measuring the interaction of the probe's magnetic field with the adjacent shock ionized flow. However, because the over-all sensitivity of the system was not great enough, performance of the conductivity gauge was marginal. Aisenberg and Chang[8] give a description of the probe and its flight data. Lennon[9] discusses the poor agreement between the conductivity gauge results and expected values as confirmed by other instruments and the theoretical analysis.

The electrostatic probe system determined electron and ion densities near the surface of the vehicle. The bias potential of some of the probes was periodically switched during flight to obtain results[2] at several distances from the surface. Analysis of probe measurement results show good agreement with flow field theory

only in the stagnation region of the nose cone. For body locations beyond the shoulder, agreement between the probe measurements and flow field theory is not so good, differences being observed for both the magnitude of the electron density and the slope of the electron density profile.

The stripline probe[7] is a new diagnostic device which consists of a lossy strip transmission line mounted on the surface of the vehicle. The outboard ground plane is omitted so that during reentry the internal fields will be affected by the dielectric properties of the flow in the boundary layer about the vehicle at the probe location. Measurement of reflection and transmission characteristics of the line give information on the plasma. Analysis of the data, now in preparation, will be reported separately.

Figure 5 shows the locations of various antennas and probes (see Table 1), with relative placement based on the behavior of the plasma sheath as predicted from previous flight data and the measurement goals of this flight; for example, probes ES-1 and ES-2 were placed on the nose cap, where agreement between predicted and measured electron density is expected to be excellent. Probes corresponding to ES-2 have been flown on all previous flights with equally good results. These two probes served as a reference for comparison of other measured data.

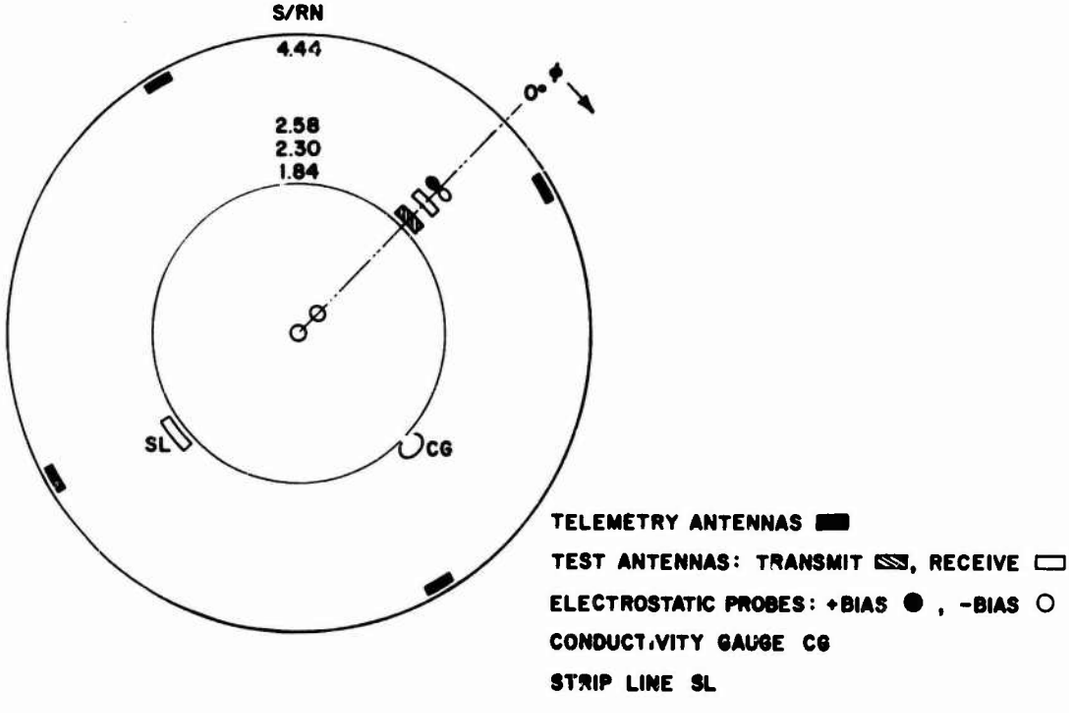

Figure 5. Head-on View of the Nose Cone Showing the Location of Antennas and Probes

Table 1. Antenna and Probe Locations and Identifications

Device	Symbol	Bias Voltage	Station (in.)	S/R_N	ϕ Clockwise
Electrostatic Probes	ES-1	Negative 15	0	0	-
	ES-2	Negative 5, 15, 30	0.70	0.47	0^o
	ES-3	Negative 5, 15, 30	12.62	2.58	4.5^o
	ES-4	Positive 15	12.62	2.58	355.0^o
Test Antenna Transmit	TX	-	8.03	1.84	0^o
Test Antenna Receive	RX	-	10.31	2.30	0^o
Telemetry Antenna	TM-1	-	24.27	4.44	105.5^o
	TM-2	-			195.5^o
	TM-3	-			285.5^o
Secondary Test/ Telemetry Antenna	TX/TM	-			15.5^o
Strip Line	SL	-	10.91	1.84	186.0
Conductivity Gauge	CG	-			90.0^o

Probes ES-3 and ES-4 were placed immediately behind the receiving antenna of the S-band test system. This allows a direct comparison between the values for the plasma properties as determined by the probes and the levels indicated by the microwave antenna results.

The location of the test antennas was chosen to ensure large plasma sheath effects on their performance, whereas the location of the telemetry antennas was to minimize the interference of the plasma sheath.

The plasma conditions around the vehicle to which the various devices are exposed depend on the over-all flight performance of the specific vehicle. In Section 3, the performance of the present flight is analyzed to establish the conditions during the test and to give a clear understanding of the flight trajectory geometry necessary to compute the radiation patterns of the test antenna. Lennon[9] gives further details that relate the performance of the present flight to that of the other two vehicles in the first phase of the AFCRL project.

3. VEHICLE FLIGHT PERFORMANCE

The flight and vehicle can be described in terms of a number of parameters that characterize the experimental payload and the over-all flight history. Table 2 summarizes these factors for the third flight. Figure 6 shows the vehicle trajectory with the significant flight events indicated. The trajectories of all the launches in the series have been quite similar, closely matching the original design goals. The time-velocity history of the reentry nose cone is shown in Figure 7. For convenience, the time-altitude history is also given here. It is seen that a peak reentry velocity of about 18,000 fps, the highest value recorded on any of the flights, was attained. Thus in comparison, the slightly greater shock strength that results for this case should produce somewhat greater heating and ionization levels. By the time the vehicle has descended to around 190 kft, the increasing air density has begun to induce significant deceleration. Below 90 kft, as is typical of all the flights, the radar tracking data became unreliable. It has not as yet been possible to resolve whether this failure can be attributed to effects based on some surface melting of the aluminum owing to aerodynamic heating, or to a break in radar tracking lock owing to the onset of high decelerations of these altitudes.

Once the fourth-stage motor had ceased its burn at around 500 kft, gravity and aerodynamically-induced drag become the only factors affecting the vehicle. The nose cone was spin-stabilized during the freefall. Because of spin and the non-zero angle of attack, changes in the vehicle orientation during reentry had a corresponding effect on the microwave transmission data and the electrostatic probe data, appearing as a modulation on the response of the devices to the external plasma (Figure 8). Precession is not observed until around 200 kft, where air density has become significant. The initial modulation is a constant 10.8 rps, due solely to vehicle spin. The aerodynamic forces below 200 kft induce an additional precession that produces an increase in the frequency of the cyclic response (Figure 8). These forces also tend to suppress the angle of attack of the nose cone. However, the spin tends to oppose this. Figure 9 shows a theoretical decay history for the angle of attack envelope, using the present vehicle parameters. The initial angle of attack α_E was about 10° and the decay from this value has been calculated as shown for both spin and no spin conditions.[9]

The relative location of the reentry nose cone with respect to the ground receiving sites is shown for three altitudes (Figure 10). As can be seen, the slant range between any site and the vehicle remained effectively constant during reentry. Thus, for the most part, it is valid to attribute changes in the received signal solely to plasma effects. Owing to the fact that the vehicle reentered almost vertically (8° flight path angle), the surface locations projected for the three altitudes are clustered together. These factors all have a bearing on interpretation of the data.

Table 2. Vehicle and Flight Parameters for Third Flight

Launch	1900 hr (EST) 24 Nov 1970	Third-stage burn time	40.8 sec
Payload weight	70.65 lb	Fourth-stage burn time	9.4 sec
W/C_DA	86.3 lb/ft^2	Initial coning: Allowed value	5.53 rps
Spin rate	11 rps	Peak velocity (at 216.5 kft)	17,972 ft/sec
I_T	0.924 slug ft^2	Initial angle of attack	10°6'
I_A	0.510 slug ft^2	Reentry flight azimuth	31°
Center of gravity (distance from nose)	9.76 in.	Time from launch to reentry (300 kft)	405.4 sec
Apogee	990,548 ft	Reentry angle (w.r.t vertical)	8.4°

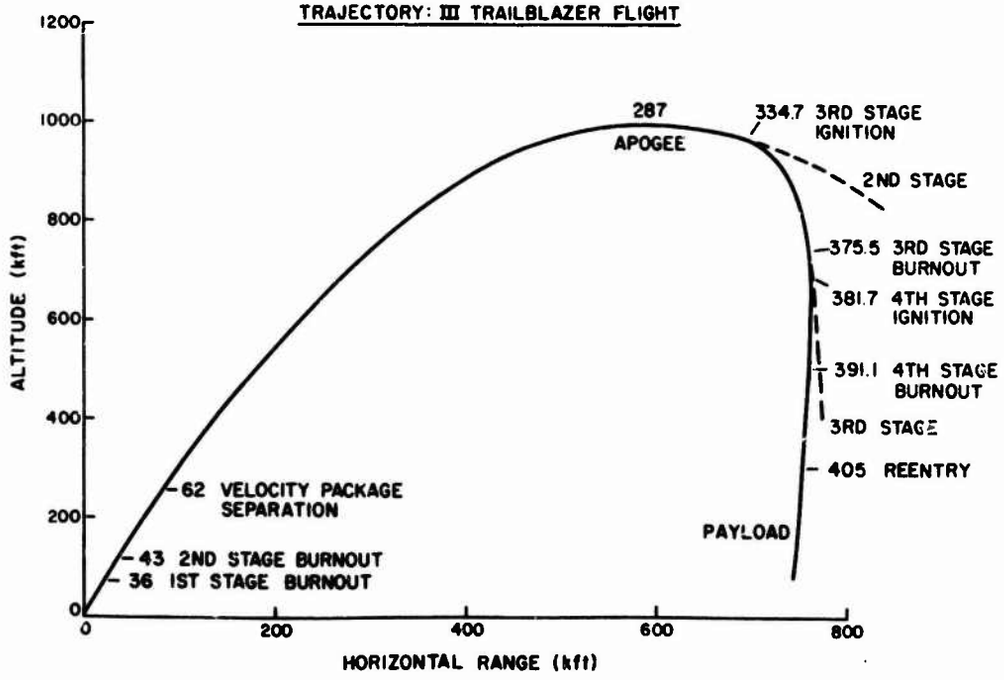

Figure 6. Flight Trajectory Showing Significant Events

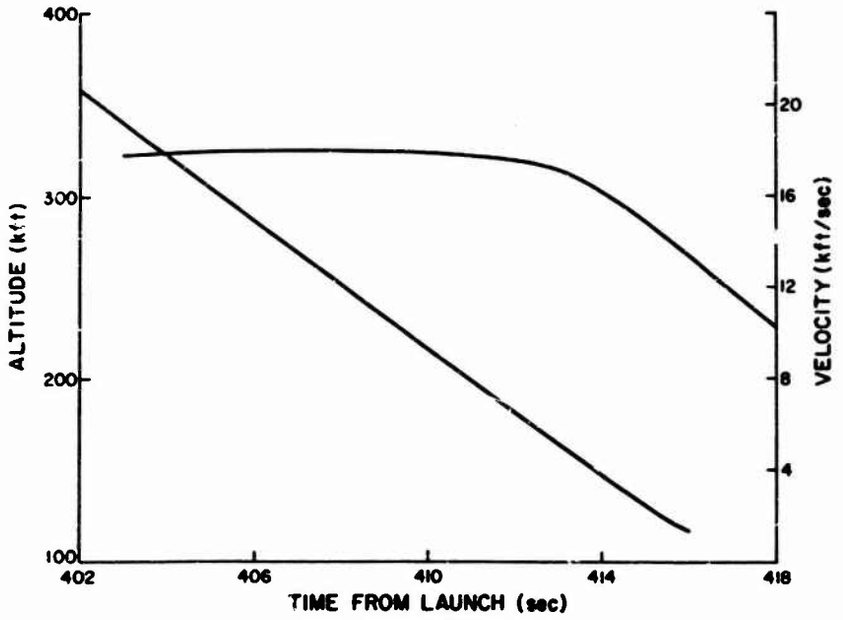

Figure 7. Time History of Altitude and Velocity

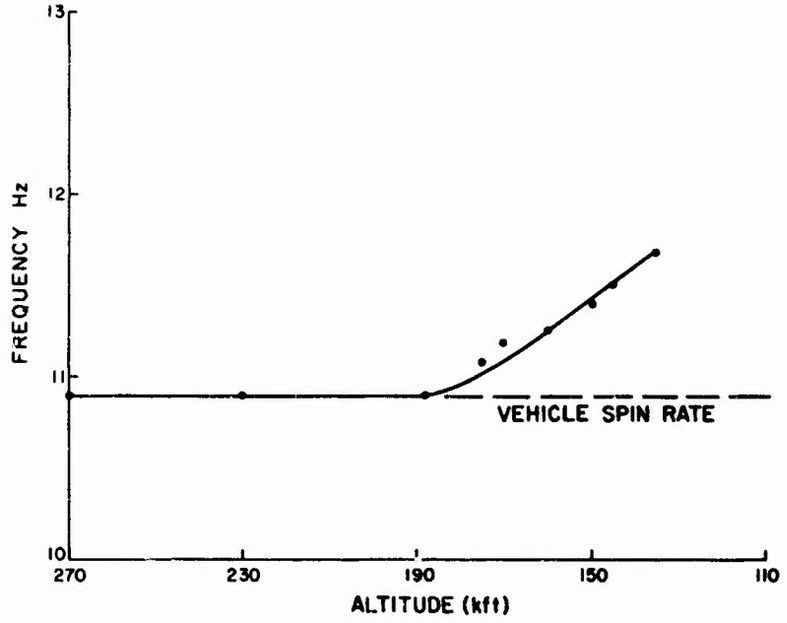

Figure 8. Frequency of Cyclic Variations in Test Data

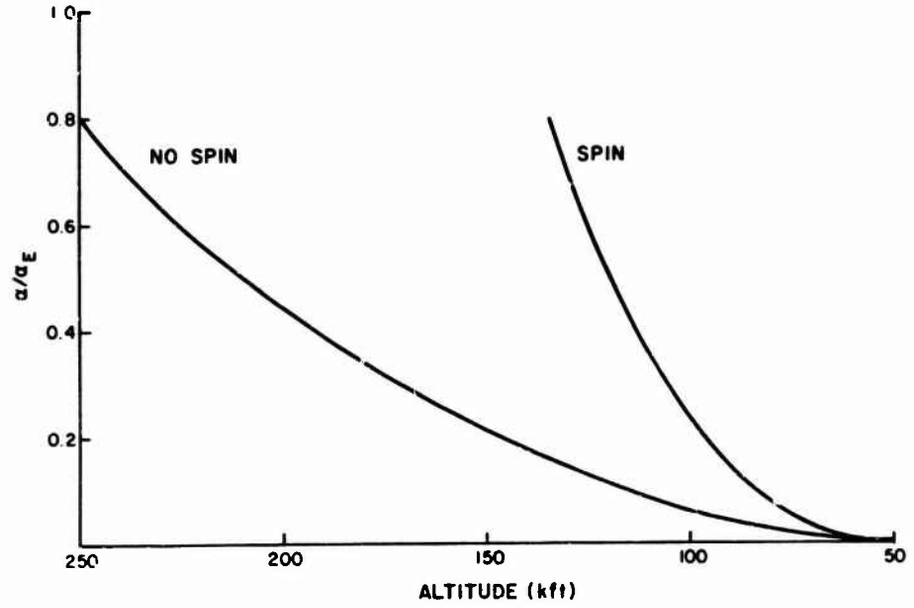

Figure 9. Decay of Angle of Attack During Reentry

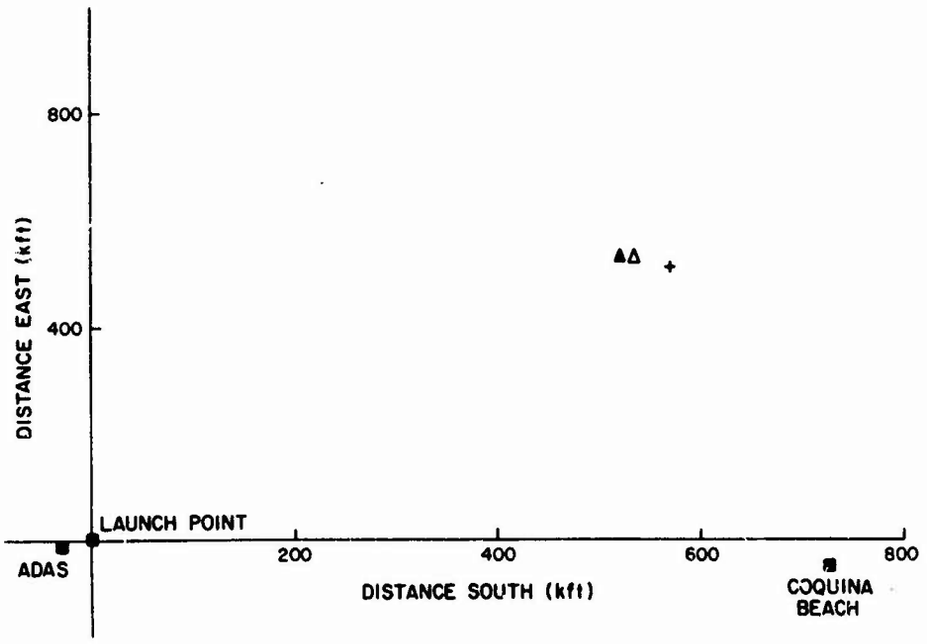

Figure 10. Geographical Orientation of Vehicle to Ground Stations During Descent. ▲ = 100 kft, Δ = 150 kft, + = 500 kft

The preceding discussion has identified the flight environment of the experiments. The next section will describe in detail the actual S-band system and the measurement techniques of the flight.

4. S-BAND TEST SYSTEM

4.1 Introduction

In this section, the primary S-band test system is described and the important in-flight measurements pointed out. A brief description of antenna performance in the presence of plasma follows with related stagnation region analyses for the previous flights outlined. Finally, the flight test results are shown and compared with predictions. The specific microwave system effects to be covered are: antenna impedance mismatch (reflection loss), interantenna coupling, antenna pattern distortion, and signal attenuation.

The predicted behavior of the S-band test system is based on theoretical flow field calculations for a similar body configuration and free steam velocity; for example, the high altitude results depend on the work of Lew.[10] Details of the various models used under the whole range of conditions, together with a full description of the technique by which these results were adapted in order to provide the necessary inputs for theoretical antenna calculations, are given in a complementary report.[11]. However, the results will be presented in a consistent form so that the basis for comparison will be clear. A block diagram of the S-band test system (Figure 11) consists of a solid-state, 2.5 W, CW transmitter connected to its antenna through a reflectometer made up of a directional coupler to sample the incident power P_{inc}, and a circulator to sample the reflected power P_{ref}. The directional coupler and circulator outputs are detected and amplified to a level (0-5 V DC) suitable for use in the telemetry system. The operating frequency was chosen as 2290.5 MHz so that standard S-band telemetry system receivers could be used at the ground receiving sites. A photograph of the S-band system components is shown in Figure 12.

The transmitting antenna was located about 2 inches behind the hemisphere-cone junction (Figure 13). Another antenna, electrically identical to the first, served as a receiving antenna; it was located farther back on the vehicle and in line with the transmitting antenna. The signal coupled into this antenna was detected, amplified

---

10. Lew, H.G. (1970) Shock Layer Ionization at High Altitudes, AFCRL-70-0702, Final Report, Contract F19628-69-C0012, GE 70SD82, The General Electric Co., Valley Forge, Penn.

11. Lennon, J.F., and Poirier, J.L. (1973) Interpretation of Microwave Antenna Results from a Reentry Flight Test: A Comparison of Methods, AFCRL.

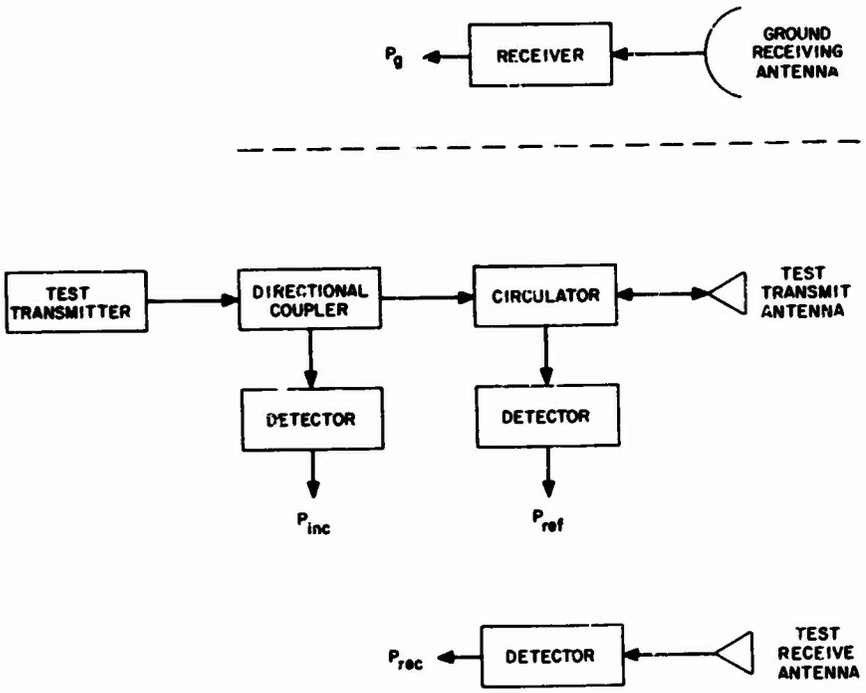

Figure 11. Block Diagram of S-Band Test System

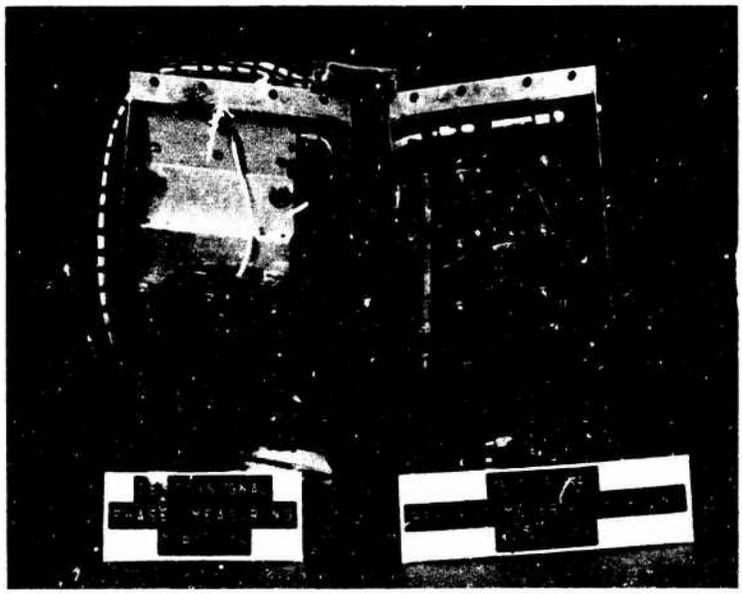

Figure 12. S-Band Test System Components

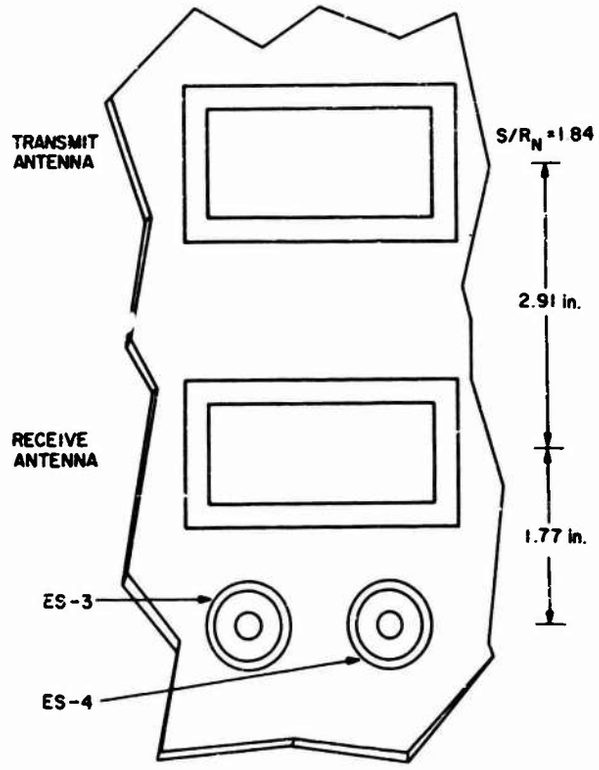

Figure 13. Cutaway View of Vehicle Surface Showing S-band Test System

to a suitable level, and transmitted to the ground over the telemetry link. Suitably normalized, the signal power at the receiving antenna terminals P_{rec} is a measure of the coupling between the receiving and transmitting antennas.

The antennas were flush-mounted cavity-backed slots, with operating characteristics that are well known and relatively easy to calculate. A sketch of the antennas (Figure 14) shows the coaxial input structure and cross-bar feed. The cavity is completely filled with hot pressed boron nitride which has a relative dielectric constant of 4. The electrical and physical properties of boron nitride make it well suited for this type of application. Table 3 gives a summary of the antenna dimensions which are used later for computing the various antenna properties of interest. The electrostatic probes ES-3 and ES-4 mounted behind the receiving antenna are also shown in Figure 13. The data from these probes have been reported previously.[2]

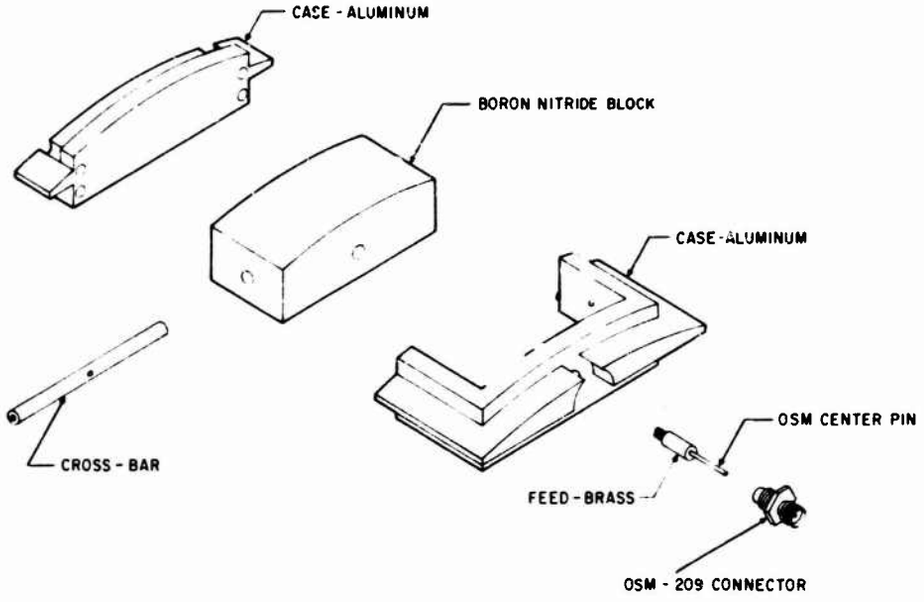

Figure 14. Sketch of Test Antenna

Table 3. Test Antenna Dimensions and Physical Characteristics

Cavity	Height	1.128 in.
	Width	2.362 in.
	Depth	0.812 in.
	Aperture radius	7.174 in.
Feed	Diameter	0.161 in.
	Distance from back wall	0.328 in.
Dielectric Material: Boron Nitride Type HD0092		
Dielectric Constant: 4		
Body Material: Aluminum		
Input Connector: OSM 209		
Terminal Impedance: 50 ohms		
VSWR: 1.5:1		
Operating Frequency: 2290.5 MHz		

4.2 Antenna System Performance in a Plasma

The operating characteristics of an antenna can be greatly affected by the presence of a plasma. Almost always, the manifestation of the antenna system-plasma interaction is a very significant or catastrophic reduction in the level of the microwave signal received from a reentry vehicle. Moreover, signals from external sources are similarly affected before they are received by antennas mounted on reentry vehicles. In addition, there are other more subtle effects which can, nevertheless, lead to equally severe degradations in system performance. Chief among these is the modification of the radiation pattern, which is often narrowed when an antenna is covered by a moderately thick plasma slab. Again, the coupling between adjacent antennas is greatly changed, an effect of importance in microwave systems employing separate transmit and receive antennas, or in multiple aperture antenna systems where a change in the mutual coupling of array elements can change the over-all radiation pattern. Usually, several of these effects are simultaneously present.

In describing the performance of an antenna system, one notes that the power reflection coefficient Γ, which is related to the magnitude of the antenna impedance mismatch, is the most direct-inflight measurement which can be made. The reflection coefficient is defined as the ratio of the reflected power P_{ref} to the incident power P_{inc}:

$$\Gamma = \frac{P_{ref}}{P_{inc}} . \tag{1}$$

The phase of the antenna impedance can also be determined, but it requires some additional measurements. As the plasma density increases, the power reflected from an initially matched antenna also increases. When the plasma frequency nears the operating frequency, a sharp increase in the power reflection coefficient takes place with most of the incident power reflected. Typical values of Γ for an overdense plasma are 0.8 to 0.9. The increase in power reflection coefficient is not monotonic, but exhibits small local minima as it nears unity.

The fraction of the signal power incident to a transmitting antenna which is received by a nearby antenna is also greatly affected by the plasma; that is, there is a substantial reduction in the received power P_{rec} as the plasma density builds up. This is due to two causes: first, the rise in the reflection coefficient of the transmitting antenna so that only part of the incident power P_{inc} is radiated; and second, an increase in the attenuation of the transmitted signal as it propagates to the receiving antenna. Therefore, the interantenna coupling loss (in dB) is defined as:

$$\text{Interantenna coupling loss} = 10 \log (P_{inc}/P_{rec}) , \tag{2}$$

and includes both internal reflection losses and external attenuation losses. The external coupling loss (in dB) is obtained by subtracting the reflection loss according to the rule

$$\text{External coupling loss} = 10 \log \frac{P_{inc} - P_{ref}}{P_{rec}} , \tag{3}$$

where P_{ref} is the power reflected from the transmitting antenna. The external coupling loss between two S-band slot antennas can be expected to change by 15 or 20 dB.

The attenuation that occurs to a signal propagated from a reentry vehicle to a ground receiving site is of critical importance in describing the operation of a microwave radiating system. The power received at a point in space depends on: first, the reflection loss due to antenna mismatch; second, the spatial distribution of the radiated power (antenna radiation pattern); and third, the attenuation of the signal as it propagates through the plasma. The first of these effects has already been discussed in connection with Eq. (1). Reflection losses of 10 dB are typical for the Trailblazer II. The last two system properties although distinct in origin, often can not be separated in effect. The signal attenuation which can reach values of 25 dB is of special concern if the signal must make a round trip traversal of the plasma, as in certain radar applications. But simultaneously there can also be a reduction (or increase) in signal strength because of a plasma-induced modification to the antenna radiation pattern. From a measurement of P_g the power received on the ground and a knowledge of the transmitted power $P_{inc} - P_{ref}$, the net signal attenuation can be found. This quantity relative to its free space value is the composite signal attenuation (CSA).

$$\text{CSA} = 10 \log \left\{ \left(\frac{P_{inc} - P_{ref}}{P_g} \right) \left(\frac{P_g}{P_{inc}} \right)_o \right\} . \tag{4}$$

The factor $(P_g/P_{inc})_o$ is the peak free-space value ($P_{ref} = 0$ with no plasma). The effect of antenna impedance mismatch is automatically removed by this definition so that the CSA depends only on the wave attenuation, the antenna radiation pattern, and the polarization relative to the receiving antenna of the wave. This last factor is involved because the actual received power P_g is used in the definition of the CSA. In the case of thin plasmas, the radiation pattern is changed little[12, 13]

12. Fante, R. L. (1967) Effect of thin plasmas on an aperture antenna in an infinite ground plane, Radio Science 2(NS)(No. 1):86-100.

13. Rotman, W. (1972) Microwave measurements of flow field characteristics at the stagnation point of a blunt reentry body, AIAA Journal Preprint, AIAA 5th Fluid and Plasma Dynamics Conference, Boston, Mass.

and Eq. (4) represents only the attenuation due to the plasma sheath. Otherwise, as for the S-band system of this flight, Eq. (4) represents the composite attenuation caused by pattern modification and signal attenuation.

It should be emphasized here that the quantities defined in Eqs. (1) through (4) all depend on the instantaneous position and orientation of the vehicle. The altitude sets the over-all plasma conditions and the orientation of the nose cone relative to the windward position accounts for angle of attack effects, determining the exact local plasma density. The signal variation due to the antenna radiation pattern of the transmitting antenna and polarization loss depend on the orientation of the nose cone relative to the ground receiving antenna. Therefore, the position and orientation of the vehicle must be specified when discussing particular values of these quantities. It will be seen that the data are given in terms of a body position (windward or leeward) or the vehicle spin angle ϕ_o for a given altitude.

4.3 Computation of Theoretical Values

The predicted values are obtained from a computer program developed by Fante.[14] This program considers a pair of slot apertures, mounted in an infinite ground plane, radiating through an inhomogeneous plasma. The quantities which are computed are the aperture admittances of the slots, the interantenna coupling, and the composite signal attenuation which includes antenna pattern modification. From this and the physical characteristics of the antenna (Table 3), the terminal impedance is obtained. The plasma is assumed to be laterally homogeneous but layered in the normal direction.

The application of the program to this flight requires some justification, particularly for the antenna radiation pattern. Discussion of these considerations and the estimation of the plasma characteristics needed as an input to the program will first be carried out.

The power received, at an arbitrary point in space, from an antenna mounted on a reentry vehicle is a complicated function of the nose cone geometry and its motion. In general, the computation of the exact fields is impossible because of the finite extent of the reentry body and the uncertainty in its motion. In practice, however, it is often possible to make certain simplifying assumptions that give good approximate values for the radiated fields and other antenna parameters of interest.

The specific motion of the reentry nose cone is quite complicated; in fact, not really known. For example, as stated in Section 3 the flight path angle was

---

14. Fante, R. L. (1971a) Reentry Antenna Test Program, Vol. 2, AVCO Systems Division Report, AVSD-0374-69-CR.

about 8° and the initial angle of attack about 10°. Precession, however, causes the vehicle axis (inclined 10° relative to the flight path) to cone about the flight path. Therefore, the angle between the vehicle axis and the line to a ground receiving site (called the local look angle) changes as the nose cone precesses. Even when the precession rate is still zero (Figure 8), the azimuthal angle of the body axis relative to the flight path is not known, and therefore the local look angle is also unknown. In addition, the aperture is inclined 9° away from the vehicle axis because the reentry vehicle is a hemisphere-cone.

Because the antenna pattern of a single slot antenna is fairly broad, these uncertainties can be overlooked; it can be assumed for the computation of the antenna patterns that the flight path is vertical and that the angle of attack is zero.

These assumptions were predicated by the uncertainty in the motion of the reentry body. Additional simplifications can be made because of the size of the nose cone compared to the wavelength. Since the cone half-angle is small, the cone may be replaced by a cylinder. Again, if the radius of the cylinder is sufficiently large, the cylinder, so far as the calculation of the radiated field is concerned, can be replaced by an infinite ground plane. This greatly simplifies the computation of the antenna pattern. Fante[15] has shown that the admittance of an axial slot aperture on a cylinder is within 20 percent of that of an identical slot on a flat ground plane when $ka = 8$. Here k is the wave number and a is the radius of the cylinder. The factor ka is equal to 8.6 for the Trailblazer II antenna being considered. The above criterion is also valid for the determination of inter-antenna coupling.

With these assumptions, the antenna fields (relative to the antenna aperture) are described in terms of a spherical-polar coordinate system (Figure 15). Here the aperture is in the x-y plane, the polar angle is limited to $\pi/2$ radians, and the origin of this coordinate system is shown in the center of the aperture. Since only the fields far from the antenna are of interest, the origin could just as well be considered to be on the central axis of the nose cone. The y axis of the antenna coordinate system is then coincident with the spin axis of the reentry vehicle. The motion of the vehicle is introduced by allowing the antenna coordinate system to rotate about another fixed system (x', y', z') which locates the nose cone. As shown in Figure 16, the y and y' axes are coincident, r is the distance from the antenna (nose cone) to the ground receiving site in the primed system, the spin angle ϕ_o measures the rotation between the two coordinate systems, and ψ is the local look angle. Because the reentry is vertical, ψ is fixed for many rotations

15. Fante, R.L. (1971b) Calculation of the admittance, isolation, and radiation pattern of slots on an infinite cylinder covered by an inhomogeneous lossy plasma, Radio Science 6(No. 3).

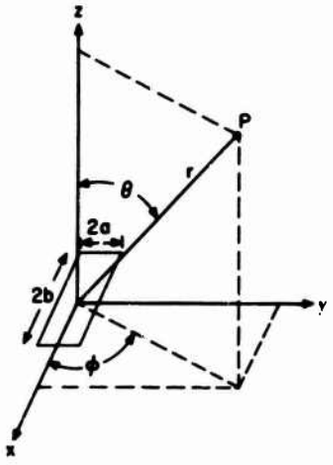

Figure 15. Coordinate System for Slot Antenna on an Infinite Ground Plane

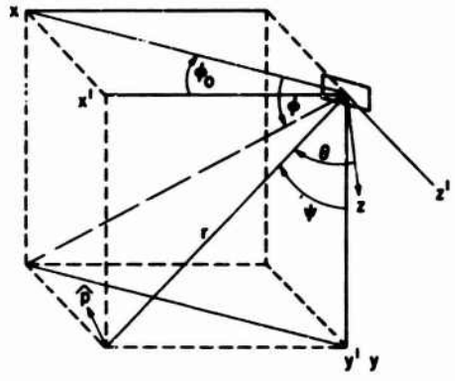

Figure 16. Coordinate System for Slot Antenna on Reentry Nose Cone

of the nose cone, varying so slowly with altitude that it can be considered constant and equal to 59° for altitudes between 250 kft and 200 kft.

The angles ϕ_o and ψ which describe the motion of the nose cone fix the angles ϕ and θ from which the antenna field is determined. The relations among these angles are most easily obtained by equating the projection of r in terms of ϕ and θ with the projection in terms of ϕ_o and ψ on each of the coordinate axes x, y, z, in turn. For the x projection, $r \sin\theta \cos\phi = r \cos\phi_o \sin\psi$. For the y projection, $r \sin\theta \sin\phi = r \cos\psi$ and for the z projection $r \cos\theta = r \sin\phi_o \sin\psi$. From these it is easy to obtain

$$\cos\theta = \sin\psi \sin\phi_o , \tag{5}$$

$$\tan\phi = \cot\psi \sec\phi_o .$$

As a final justification for using the flat plate model, the free space radiation pattern of the nose cone is compared to the theoretical flat plate pattern (Eq. A3) in Figure 17 for $\psi = 90^{\circ}$. As can be seen there is good agreement between the two for $10 < \phi_o < 170^{\circ}$. The flat plate pattern is always zero for $180^{\circ} < \phi_o < 360^{\circ}$, so only the front lobe of the antenna pattern is of interest in this model.

The specific calculations which are required to determine the flow field properties at each altitude are found in the work of Lew[10] and Lennon.[9] The results of these calculations based on vibrational equilibrium give the electron

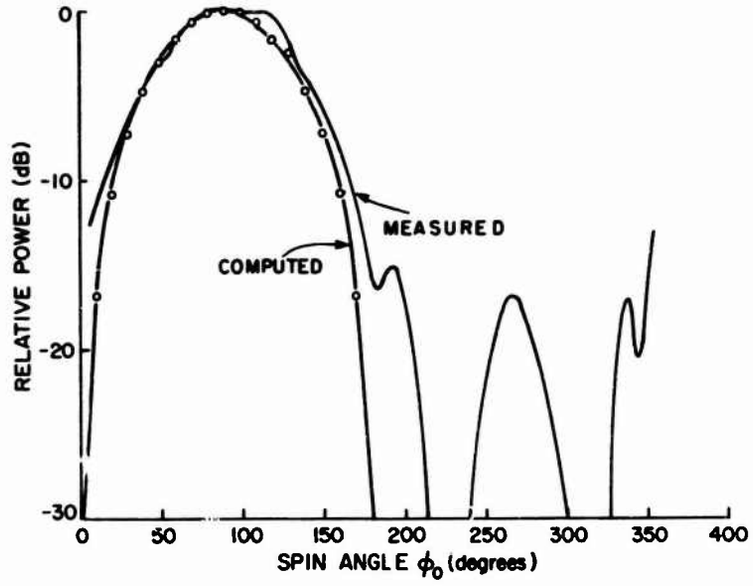

Figure 17. Comparison of Computed Pattern for Slot on Flat Ground Plane and Measured Pattern for Reentry Nose Cone. $\psi = 90^{o}$. Receiver polarization-vertical linear.

density and collision frequency profiles of the plasma as a function of altitude for various body locations. The variation in plasma properties in the normal direction is taken into account by using a layered model where the properties within a layer are uniform, changing only between slabs. The plasma is assumed homogeneous in the lateral direction. The division of the computed electron density and collision frequency profiles into slabs is shown in Table 4 for the eight altitudes for which the patterns were computed.

Using these plasma properties and the physical characteristics of the transmitting antenna, one computes the signal attenuation as a function of ϕ_o for each altitude of interest. The results for $\psi = 59^{o}$ are shown in Figure 18 indicating that significant changes can be expected in the attenuation patterns with changes in altitude. In these calculations the attenuation refers to the reduction (over the free-space value) in the power radiated by the vehicle antenna as observed by a completely polarized receiving antenna on the ground.

The comparison of the computed antenna system parameters with those which were observed during the flight can now be carried out.

Table 4. Plasma Properties at Test Antenna Body Location. $S/R_N = 1.84$

Altitude kft	Slab Thickness cm	Electron Density $el/cm^3 \times 10^{-10}$	Collision Frequency $1/sec \times 10^{-8}$
240	0.10	0.41	3.37
	0.19	0.76	2.49
	0.29	0.96	2.15
	0.37	1.08	1.90
	0.42	1.12	1.77
	0.46	1.07	1.74
	0.49	0.84	1.71
	1.35	0.59	1.67
	0.78	0.19	1.58
	0.72	0.03	1.56
235	0.29	1.00	3.01
	0.84	2.10	2.00
	1.12	2.25	1.83
	1.12	1.40	1.68
	0.56	0.38	1.60
230	0.32	1.90	3.44
	0.88	3.90	2.35
	1.22	3.90	2.10
	1.22	2.20	1.93
	0.61	0.45	1.83
225	0.37	3.40	3.91
	1.03	6.80	2.75
	1.42	6.60	2.44
	1.42	3.10	2.22
	0.71	0.48	2.08
220	0.55	9.00	3.50
	0.75	11.00	3.25
	1.00	11.00	2.95
	1.00	9.60	2.80
	1.00	6.30	2.60
	1.00	2.75	2.50
	1.00	0.84	2.40
	1.00	0.15	2.30
	1.00	0.01	2.30
215	0.48	9.00	5.00
	1.32	16.00	3.85
	1.82	14.50	3.30
	1.82	4.60	2.96
	0.91	0.48	2.65

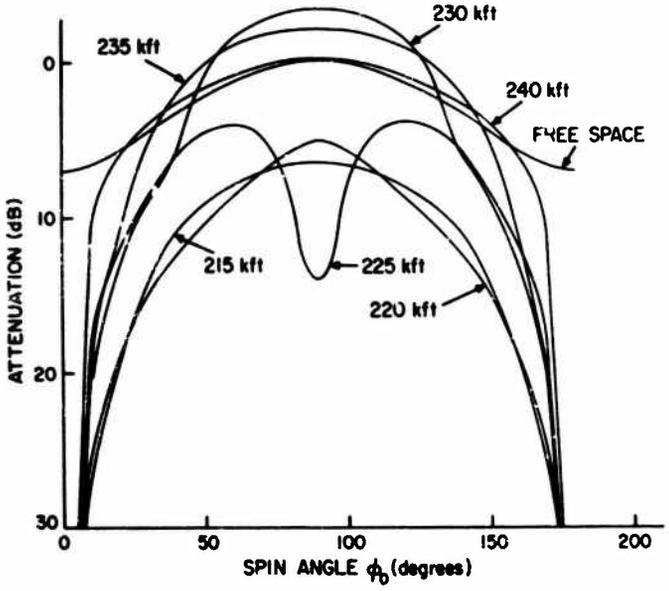

Figure 18. Computed "Amplitude Patterns" for Plasma Covered Slot Antenna

5. FLIGHT TEST RESULTS

As previously mentioned, a non-zero angle of attack caused the plasma, as seen by a point on the vehicle surface, to vary as the nose cone rotated. This introduced a corresponding variation in any microwave measurement sensitive to a change in plasma conditions between the windward and leeward sides. For comparison therefore, the results are presented in terms of the same angular point for each spin cycle. The windward or leeward sides do not necessarily correspond to the positions of maximum or minimum effect. Often intermediate locations produce larger variations.

The reduced flight data for the power reflection coefficient, caused by the antenna impedance mismatch, is shown as a function of time (Figure 19). Here only the values for the windward and leeward sides have been plotted. As indicated, for a given altitude during its build-up period, the power reflection coefficient was always larger on the windward side than on the leeward side. Once the plasma frequency on both sides reached the operating frequency, the variation in antenna response diminished greatly. Beyond 413 sec the telemetry signal (this data was transmitted over the telemetry link) became intermittent and some reflection coefficient data points were missed. Also plotted here is the theoretical power reflection coefficient obtained from the computer program.

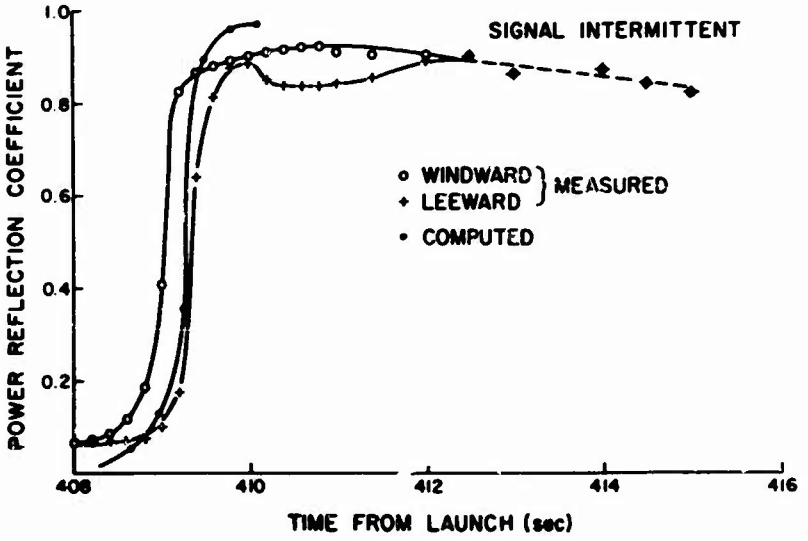

Figure 19. Power Reflection Coefficient

It is especially important to notice that the predicted value, computed for zero angle of attack, falls between the measured responses of the windward and leeward sides.

The operational significance of this antenna mismatch (detuning) is better appreciated when given in terms of an equivalent reduction in transmitted signal. The effective reduction in signal strength due to antenna impedance mismatch is plotted in Figure 20. Values in excess of 10 dB are observed for the overdense plasma.

The interantenna coupling loss defined by Eq. (2) is plotted in Figure 21 for the windward and leeward vehicle positions. As indicated the coupling loss at first decreased slightly and then rose sharply as the plasma density increased. During the buildup period the decrease in antenna coupling was always less on the leeward side than on the windward side except for a short period at the onset of plasma conditions. The theoretical value, it is seen, agrees closely with the measured response and again falls between the windward and leeward sides. Changes of greater than 25 dB are observed in interantenna coupling loss.

The interantenna coupling loss however includes the effect of internal reflection at the transmitting antenna. In Figure 22, the coupling loss characteristic of the external propagation is plotted. The external coupling loss has the same general characteristics as the interantenna coupling loss except for a reduction in the magnitude in the overall change in coupling. Again, the zero angle of attack computed curve falls between the windward and leeward body positions.

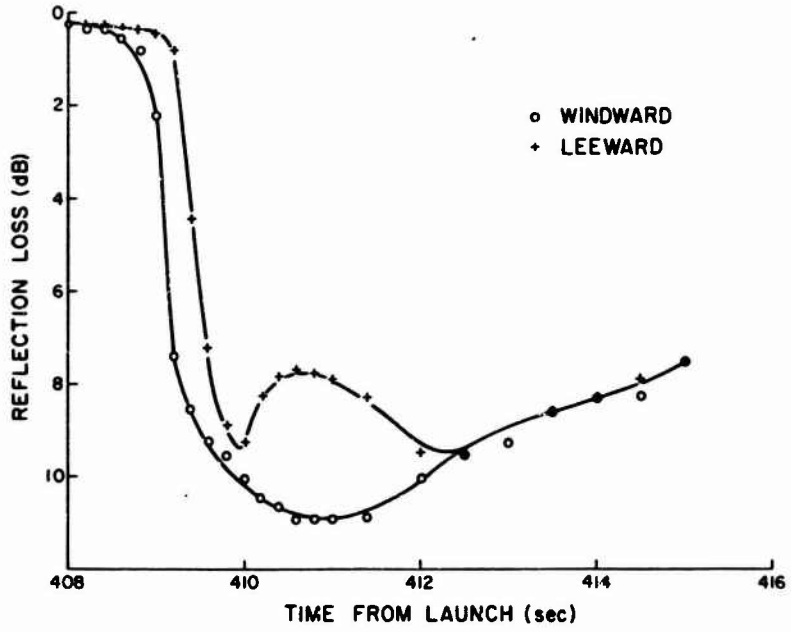

Figure 20. Plasma Induced Reflection Loss

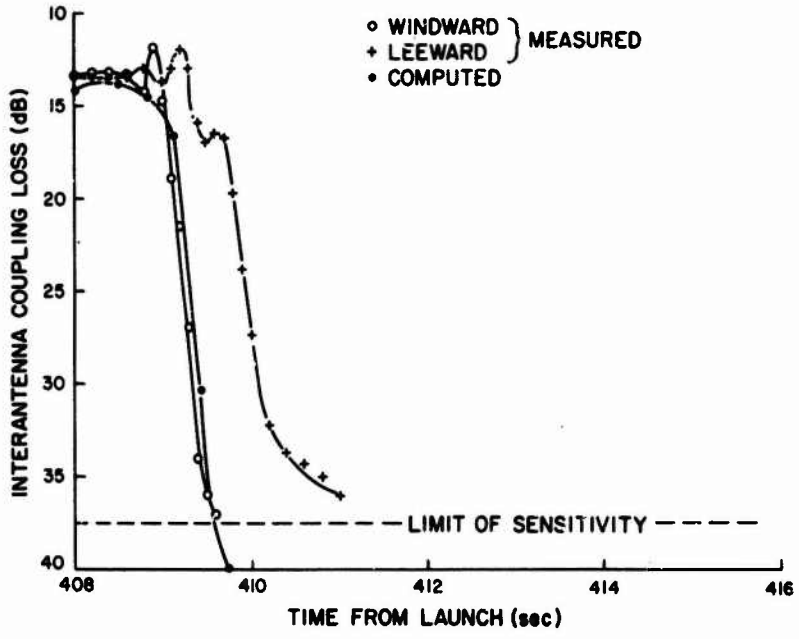

Figure 21. Interantenna Coupling Loss

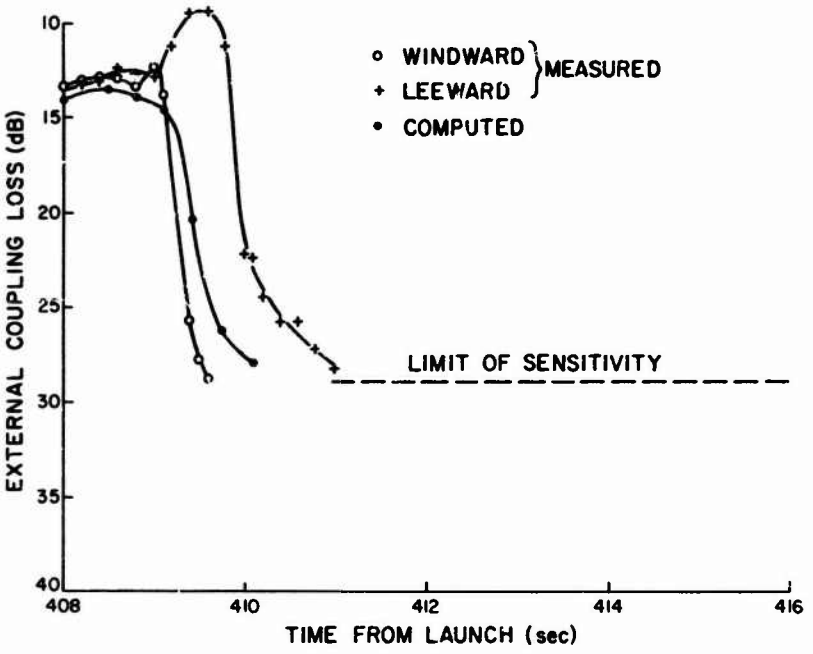

Figure 22. External Coupling Loss

At the ground receiving sites, the signal strength of the test signal was measured by recording the receiver agc voltage. These records can provide an estimate of the composite signal attenuation caused by the plasma sheath. The magnitude of the agc voltage varied with spin since this changed the antenna orientation relative to the ground station. The resulting pattern showed one main lobe characteristic of a single slot antenna. The back lobe, however, was not evident even at altitudes sufficiently high to ensure that no plasma effects yet existed. This distortion was introduced by the ground station receivers because the frequency response of the agc loop was too low to follow the antenna pattern variations of the spinning vehicle.

The CSA for the peak value ($\phi_o = 90^o$) of the received signal was obtained from Eq. (4). From the agc signal the received signal power P_g and the time of occurrence of the peak were determined. The incident power P_{inc} and the reflected power P_{ref} corresponding to this time were then found from the telemetry data. Firally, the factor $(P_g/P_{inc})_o$ was obtained by noting the values of the quantities just before reentry. The result of this exercise is plotted in Figure 23 and shows that there is an increase of greater than 25 dB in the composite signal attenuation when the plasma builds up. The slight decrease in attenuation

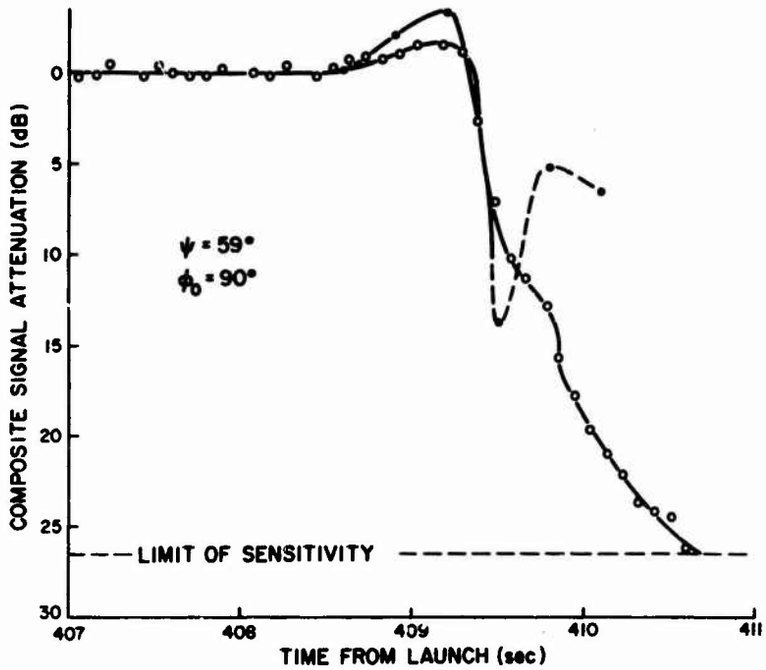

Figure 23. Composite Signal Attenuation.

at plasma onset is due to a narrowing of the antenna radiation pattern. The theoretical values are obtained from the attenuation patterns of Figure 18 sampled for $\phi_o = 90$. Inspection of Figure 23 reveals the excellent agreement between the computed and measured values during the initial buildup. However, the computed curve shows a strong resonance as the plasma becomes critical. At this point, there is first a sharp decrease in the attenuation, quickly followed by a more gradual increase toward the measured value. The measured curve shows a perturbation during this period, also indicating the existence of a resonance phenomenon.

The amplitude of a computed resonance effect critically depends on the detailed plasma conditions at that instant, and very small changes in plasma properties produce a large change in response. The model used for these calculations only approximates the actual detailed plasma conditions. For example, in an actual flight, the plasma properties which are neither homogeneous nor isotropic, are also changing because the nose cone altitude is steadily decreasing. Superimposed on this, is a cyclical variation induced by the vehicle spin and the non-zero angle of attack. In contrast, the model

assumes plasma properties that are laterally homogeneous and isotropic, frozen in time, and independent of spin angle (zero angle of attack). For these reasons the computed curve is not a good representation of the CSA in the neighborhood of the resonance. As a reminder of this, the computed curve in Figure 23 is dashed in this region.

Theoretical values for lower altitudes are now being computed and will be presented in another report.[11] It is expected that away from the resonance there will again be good agreement between the computed and measured values.

The CSA as a function of spin angle ϕ_o is called the composite signal attenuation pattern and graphically represents the variation with spin of the received signal power as the plasma builds up. The measured values are easy to obtain from the agc records and the corresponding values of radiated power (as was done for Figure 23). The variation in the measured value depends on the polarization characteristics of the receiving antenna system at the ground receiving site. In contrast, the computed curves shown in Figure 18 give the signal power which would be received by a completely polarized system. Therefore, these curves must first be modified to reflect the polarization properties of the receiving antenna before they can be compared to the measured curves. This added computation is not necessary here since the ground receiving antennas had circular polarization. The measured and computed CSA patterns are compared in Figure 24 for several altitudes. In evaluating these curves it should be kept in mind that the nose cone antenna pattern has a back lobe and the flat-plate model does not. Only the attenuation for $0 < \phi_o < 180$ then is to be compared. In addition, for $\phi_o \approx 0$ and $\phi_o \pm 180^o$, the propagation path (in the model) is at a grazing angle and stays within the plasma slab literally. At these angles the flat-plate model does not adequately represent the real plasma covered nose cone and predicts too much attenuation. For this reason, the region of comparison is restricted to the spin angles $10^o < \phi_o < 170^o$. It should also be remembered that the long time constant of the agc loop response caused severe distortion of the measured data in the region of the back lobe. Nevertheless, comparison of the computed and measured curves for the three highest altitudes shows good agreement so far as attenuation pattern narrowing and increase in received signal at plasma onset are concerned.

The pattern at 225 kft is particularly interesting; it corresponds to the system going through plasma resonance. This effect occurs over a very narrow altitude range. The computed value assumes that the plasma properties remain constant during an entire spin cycle. In reality the plasma properties are changing with altitude during a spin cycle. At 225 kft, there is an altitude change of about 1.5 kft during one revolution. The resonance effect observed in Figure 24d occurs only over an altitude range of about 3000 ft. It is not surprising then that the location

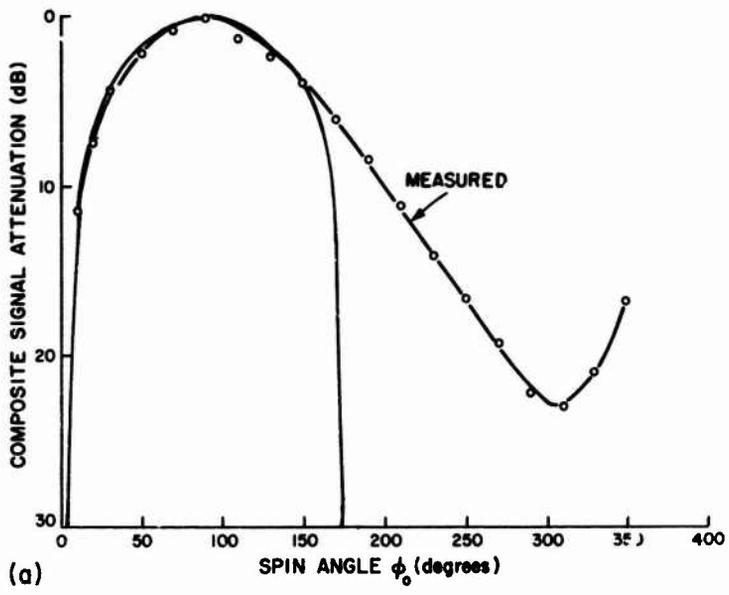

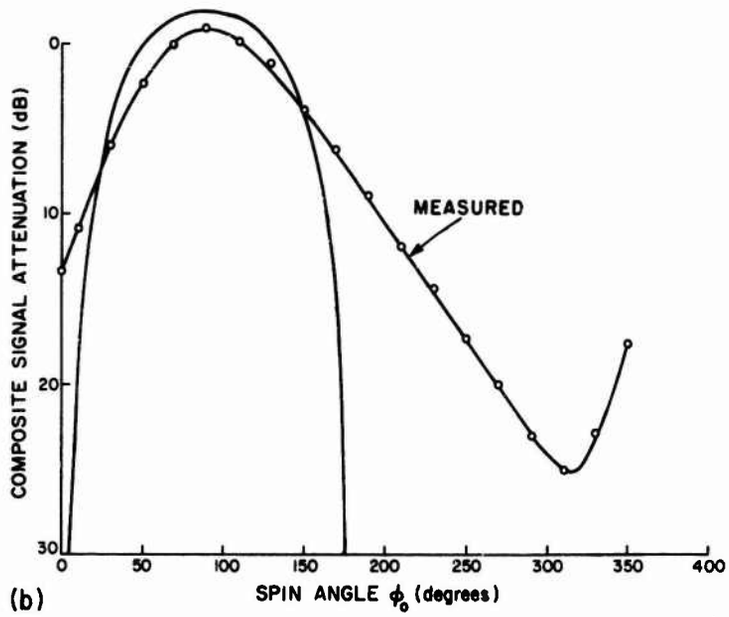

Figure 24. Composite Signal Attenuation . $\psi = 59^{o}$ (a) 240 kft, (b) 235 kft

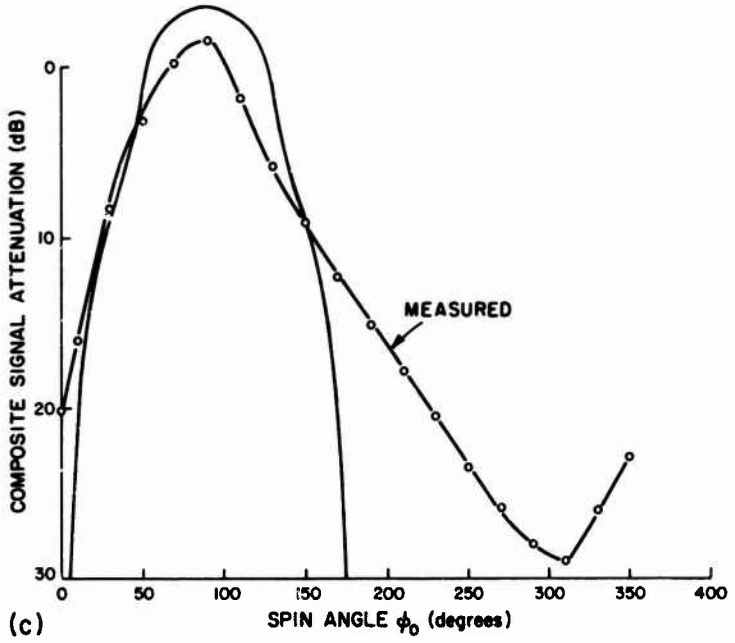

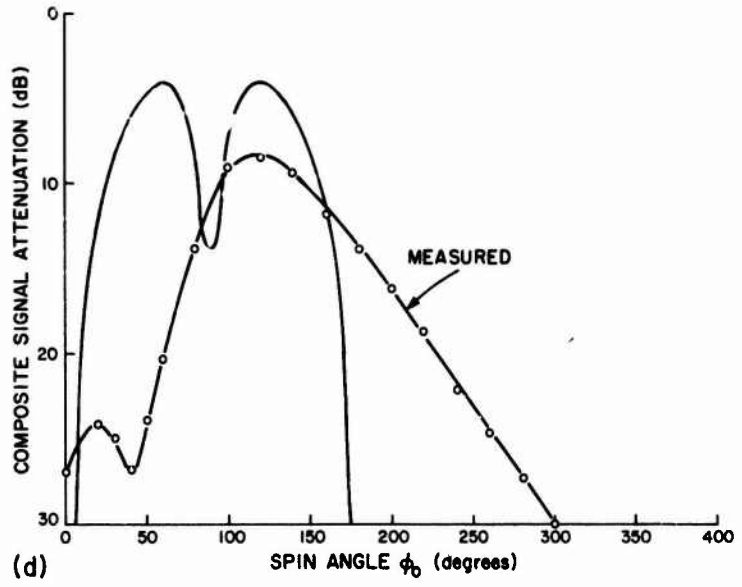

Figure 24 (Contd.). Composite Signal Attenuation. $\psi = 59^{\circ}$ (c) 230 kft, (d) 225 kft

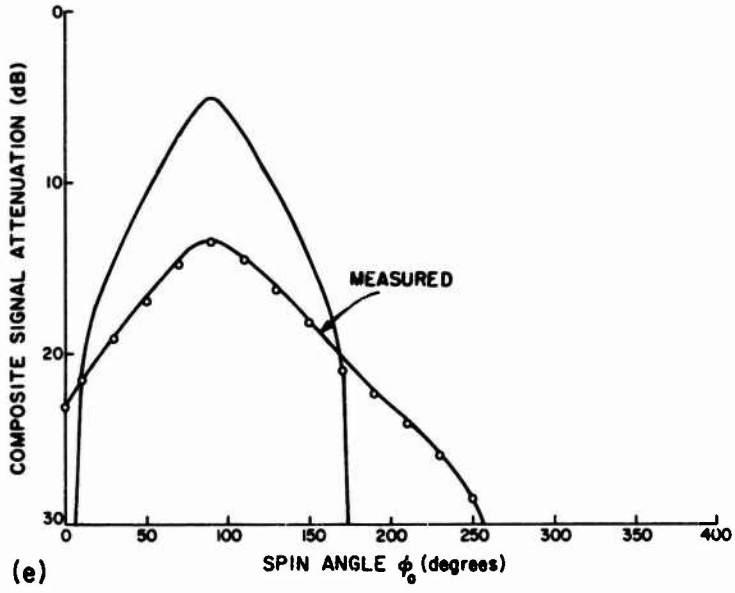

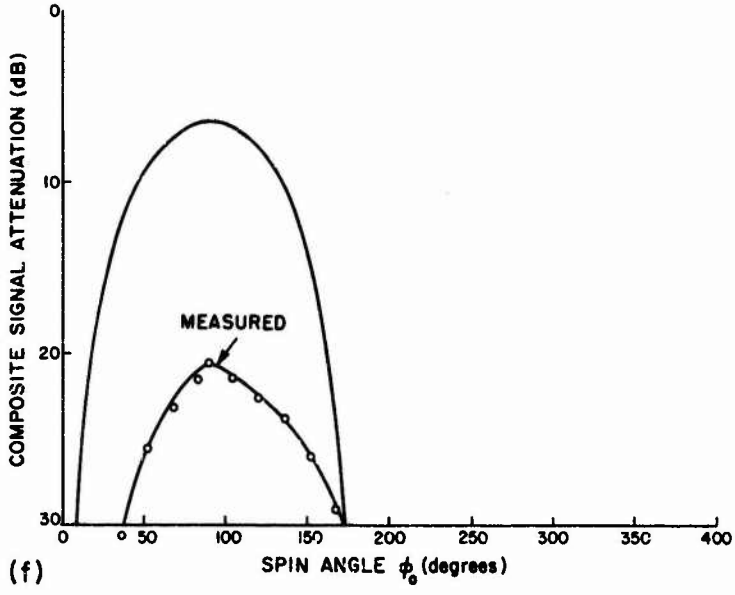

Figure 24 (Contd.). Composite Signal Attenuation. $\psi = 59^{o}$ (e) 220 kft, (f) 215 kft

of the resonance and the relative amplitude of the two peaks are different. The important result here is that a resonance effect was indeed observed. It should also be remembered, as discussed in connection with Figure 23, that the computed values in the neighborhood of plasma resonance may not adequately represent the true conditions.

Inspection of the agc records discloses that the indicated signal strength from the back lobe decreases more rapidly with plasma buildup than does the signal from the main lobe. Although the absolute difference is subject to question because of the distortion in the records, the trend is apparent. Figure 25 shows a plot of the ratio of the front lobe to back lobe received power. This larger drop in the back lobe power is to be expected, since the signal must propagate over a longer path in the plasma for this condition.

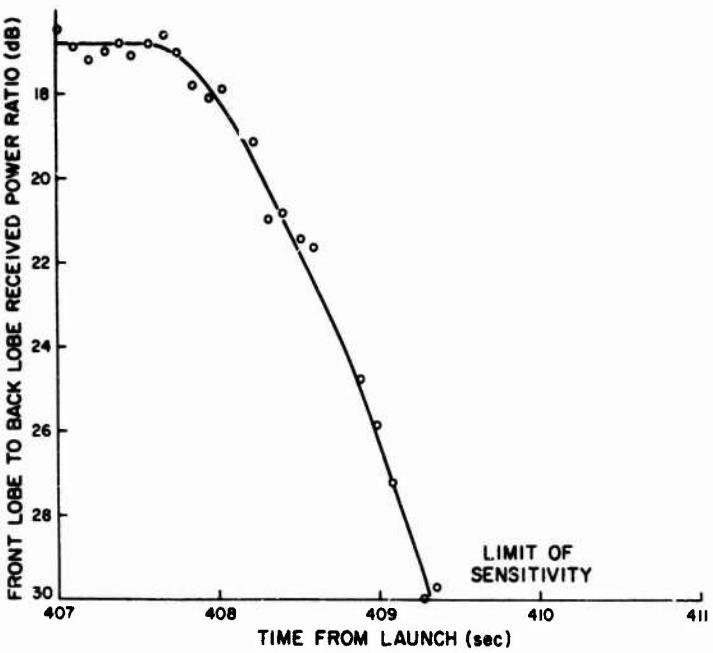

Figure 25. Comparison of Composite Signal Attenuations of Front Lobe and Back Lobe. $\psi = 59^{o}$, $\phi_o = 90^{o}$ (Main Lobe), $\phi_o = 180^{o}$ (Back Lobe)

6. SUMMARY

To study the effects of shock ionized air on the performance of a microwave system, the goal of the flight, has been achieved, as substantiated by the experimental data presented in this report. It has also been shown that the theoretical computations of antenna operation are in good agreement with experiment. This means that not only must the models used for the antenna calculations be reasonably good, but that flow fields used as inputs for these calculations must be equally good representations of the true conditions.

In particular, the measured and computed values of antenna impedance mismatch and interantenna coupling agreed closely for the entire flight. Similar agreement was obtained for the composite signal attenuation for altitudes above 225 kft. At this altitude, however, the strong resonance which occurs in the computed data causes a marked difference between theory and observation. More computations at lower altitudes are now being carried out, and it is expected that these new results will again agree with observation.

During this flight, measurements were also made of electron and positive ion density, and reported separately.[2] These results can now serve as a standard against which to measure the effectiveness of various chemical additives to eliminate the performance limitations imposed by the plasma. Now the measurements made with additives during reentry can be compared with computed values (without additives) obtained from a tested theory. One of these chemical alleviation flights[3] in which Freon 114B2 was used as the additive, showed significant improvement in antenna operation over similar flights without additive.

References

1. Poirier, J.L., Rotman, W., Hayes, D.T., and Lennon, J.F. (1969) Effects of the Reentry Plasma Sheath on Microwave Antenna Performance: Trailblazer II Rocket Results of 18 June 1967, AFCRL-69-0354.

2. Hayes, D.T. (1972) Electrostatic probe measurements of flow field characteristics of a blunt body reentry vehicle. Presented at 5th Fluid and Plasma Dynamics Conference, Boston, Mass., AIAA Paper 72-694.

3. Hayes, D.T., Herskovitz, S.B., Lennon, J.F., and Poirier, J.L. (1972) Preliminary Report on the Trailblazer II Chemical Alleviation Flight of 28 July 1972, AFCRL-72-0640.

4. Rotman, W., and Maloney, L.R. (1973) High Power Microwave Antenna Performance in the Stagnation Region of a Blunt Reentry Nose Cone, AFCRL-TR-72-0072.

5. Hayes, D.T., and Rotman, W. (1973) Microwave and electrostatic probe measurements and a blunt reentry vehicle, AIAA Journal 11(No. 5):675.

6. Lustig, C.D., and Hayes, D.T. (1969) Observation of electroacoustic resonance in a reentry sheath, Proc. IEEE 57(No. 5):800-802.

7. Karas, N.V. (1972) Microstrip Plasma Probe [illegible]CRL-72-0417.

8. Aisenberg, S., and Chang, K.W. (1971) C[illegible]dditives and Diagnostics for High Temperature Air F[illegible]. AFCRL-62-0354, Final Report, Contract F19628-71-C-0077

9. Lennon, J.F. (1972) Trailblazer II Rocket Tests on the Reentry Plasma Sheath: Vehicle Performance and Plasma Predictions (Flights No. 1-3), AFCRL-TR-73-0317.

10. Lew, H.G. (1970) Shock Layer Ionization at High Altitudes, AFCRL-70-0702, Final Report, Contract F19628-69-C0112, GE 70SD782, The General Electric Co., Valley Forge, Penn.

11. Lennon, J.F., and Poirier, J.L. (1973) Interpretation of Microwave Antenna Results from a Reentry Flight Test: A Comparison of Methods, (To be published).

12. Fante, R.L. (1967) Effect of thin plasmas on an aperture antenna in an infinite ground plane, Radio Science 2(NS)(No. 1):86-100.

13. Rotman, W. (1972) Microwave measurements of flow field characteristics at the stagnation point of a blunt reentry body, AIAA Journal Preprint, AIAA 5th Fluid and Plasma Dynamics Conference, Boston, Mass.

14. Fante, R.L. (1971a) Reentry Antenna Test Program, Vol. 2, AVCO Systems Division Report, AVSD-0374-69-CR.

15. Fante. R.L. (1971b) Calculation of the admittance, isolation, and radiation pattern of slots on an infinite cylinder covered by an inhomogeneous lossy plasma, Radio Science 6(No. 3).

16. Collin, R.E., and Zucker, F.J. (1969) Antenna Theory, Part 1, McGraw Hill, New York.

Appendix A

Slot Aperture Radiation Fields

The electric fields $\vec{E}_\phi$ and $\vec{E}_\theta$ radiated by a slot with a uniform aperture distribution in the narrow direction and a cosinusoidal distribution in the broad dimension are[16] for an infinite ground plane:

$$\vec{E}_\phi = \hat{\phi}\, A \cos\phi \cos\theta \text{ and } \vec{E}_\theta = \hat{\theta}\, A \sin\phi \,. \tag{A1}$$

The fields are defined in terms of the coordinate system in Figure 15; the caret indicates a unit vector, and

$$A = ikE_o ab \exp[-ikr] \frac{\sin(ka \sin\phi \sin\theta)\cos(kb\cos\phi\sin\theta)}{rka \sin\phi \sin\theta \left[(kb\cos\phi\sin\theta)^2 - (\pi/2)^2\right]^{1/2}} . \tag{A2}$$

The relative power radiated in any direction is found from the relation

$$P(\theta,\phi) = \frac{(\vec{E}_\phi + \vec{E}_\theta)\cdot(\vec{E}_\phi^* + \vec{E}_\theta^*)}{\left[(\vec{E}_\phi + \vec{E}_\theta)\cdot(\vec{E}_\phi^* + \vec{E}_\theta^*)\right]_{max}} . \tag{A3}$$

---

16. Collin, R. E., and Zucker, F. J. (1969) Antenna Theory, Part I, McGraw Hill, New York.

★ U.S. GOVERNMENT PRINTING OFFICE: 1974-704-296/67